2014

Understanding the pharmacological properties of a metabolic PET tracer in prostate cancer

Nerissa Therese Viola-Villegas

Sean D. Carlin

See next page for additional authors

Citation/Publisher Attribution

Viola-Villegas, N., Carlin, S. D., Ackerstaff, E., Sevak, K. K., Dilov, V., Serganova, I., Kruchevsky, N.,...Lewis, J. S. (2014). Understanding the pharmacological properties of a metabolic PET tracer in prostate cancer. *Proc. Acad. Natl. Sci., 111*(20), 7254-7259. doi: 10.1073/pnas.1405240111
Available at: https://doi.org/10.1073/pnas.1405240111

Authors

Nerissa Therese Viola-Villegas, Sean D. Carlin, Ellen Ackerstaff, Kuntal K. Sevak, Vadim Divilov, Inna Serganova, Natalia Kruchevsky, Michael Anderson, Ronald G. Blasberg, Oleg A. Andreev, Donald M. Engelman, Jason A. Koutcher, Yana K. Reshetnyak, and Jason S. Lewis

Understanding the pharmacological properties of a metabolic PET tracer in prostate cancer

Nerissa Therese Viola-Villegas[a,b], Sean D. Carlin[a,b], Ellen Ackerstaff[c], Kuntal K. Sevak[b], Vadim Divilov[b], Inna Serganova[d], Natalia Kruchevsky[c], Michael Anderson[e], Ronald G. Blasberg[a,b,d], Oleg A. Andreev[e], Donald M. Engelman[f,1], Jason A. Koutcher[a,b,c,g], Yana K. Reshetnyak[e], and Jason S. Lewis[a,b,1]

[a]Program in Molecular Pharmacology and Chemistry, and Departments of [b]Radiology, [c]Medical Physics, [d]Neurology, and [g]Medicine, Memorial Sloan–Kettering Cancer Center, New York, NY 10065; [e]Department of Physics, University of Rhode Island, Kingston, RI 02881; and [f]Department of Molecular Biophysics and Biochemistry, Yale University, New Haven, CT 06520

Contributed by Donald M. Engelman, March 28, 2014 (sent for review November 24, 2013)

Generally, solid tumors (>400 mm^3) are inherently acidic, with more aggressive growth producing greater acidity. If the acidity could be targeted as a biomarker, it would provide a means to gauge the pace of tumor growth and degree of invasiveness, as well as providing a basis for predicting responses to pH-dependent chemotherapies. We have developed a $^{64}\mathrm{Cu}$ pH (low) insertion peptide (pHLIP) for targeting, imaging, and quantifying acidic tumors by PET, and our findings reveal utility in assessing prostate tumors. The new pHLIP version limits indiscriminate healthy tissue binding, and we demonstrate its targeting of extracellular acidification in three different prostate cancer models, each with different vascularization and acid-extruding protein carbonic anhydrase IX (CAIX) expression. We then describe the tumor distribution of this radiotracer ex vivo, in association with blood perfusion and known biomarkers of acidity, such as hypoxia, lactate dehydrogenase A, and CAIX. We find that the probe reveals metabolic variations between and within tumors, and discriminates between necrotic and living tumor areas.

The rapid growth and division of tumor cells create an enhanced need for glucose and other nutrients, which the cells take up at a high rate, overwhelming their mitochondrial capacity to use all of the glucose efficiently (1). The result is aerobic glycolysis, which elevates lactate and proton production: the "Warburg" effect (1, 2). Further, some tumors are starved for oxygen, resulting in even more glycolytic acid production (3, 4). Under the resulting low pH conditions, normal cells have a tendency to undergo p53-induced apoptosis (5, 6), whereas cancerous cells invoke alternative routes, manipulating ion fluxes with proton extruders and other transporters to afford continuous survival (7). Pumping the acidic components out of the cell maintains cytoplasmic pH and enhances the pH gradient (ΔpH), and the cellular exterior surfaces become more acidic than those of cells in normal tissues (8). The level of extracellular acidification, however, is variable, depending on (*i*) the reliance of the malignancy on glycolysis (9–11), a phenomenon resulting from the pleiotropic adaptation of cancer cells toward a glycolytic phenotype; (*ii*) the impact of variation in the distal vascular delivery of nutrients; and (*iii*) the state of hypoxia (12, 13). The low pH environment stimulates cell invasion, angiogenesis, and, finally, metastasis (14, 15).

Tumor extracellular acidosis could be a useful biomarker for selective drug delivery, targeting, and delineation of malignancies. With the discovery of a membrane-inserting pH (low) insertion peptide (pHLIP) that preferentially binds to cell membranes at low extracellular pH (pHe), practical clinical imaging and delivery of therapeutic payloads may be possible (16–18). At normal pH, pHLIP binds as a largely unstructured peptide at a membrane surface, but at acidic pH, it folds and inserts across the plasma membrane as an α-helix (19). We have previously demonstrated that pHLIP might be useful as a PET probe with $^{64}\mathrm{Cu}$ ($t_{1/2} \sim 12.7$ h) (20). Tumor uptake in prostate cancer models was achieved, and related to low pHe, but shortcomings were apparent (20). The success of the probe as a marker of acidosis was found to have contrast and clearance complexities associated with the pharmacokinetics (PK) of pHLIP, warranting further development efforts. Targeting of fluorescent pHLIP variants was recently studied, and a range of potential properties was found, including altered kinetics of insertion (21) (Scheme S1). Here, we describe a much improved PET probe that was developed using three strategies: modification of the (*i*) peptide sequence, (*ii*) radiometal, and (*iii*) chelate. We confirmed the lead radiotracer's specificity for a low pH gradient by demonstrating an association between pHLIP-PET and pHe in different prostate cancer models: (*i*) PC3-wt cells, (*ii*) the constitutively expressing carbonic anhydrase IX (CAIX)-transduced PC3 cells, and (*iii*) LNCaP cancer cells. Lastly, we extended our study by offering a representative relationship of pHLIP with perfusion, tumor viability, and pathways associated with acidity [i.e., lactate via the lactate dehydrogenase A (LDH-A) protein subunit, hypoxia, CAIX overexpression]. The probe gives useful contrast, reveals metabolic variations within tumors, and discriminates between necrotic and living tumor areas.

Results

Appropriate Peptide Sequence, Radionuclide, and Chelating Ligand Modifications Can Significantly Improve pHLIP-PET Properties. We made several modifications to reduce the nonspecific binding of the PET probe to normal tissues to maximize contrast while

Significance

Solid tumors adapt a glycolytic phenotype for their energetic requirements, leading to acidification of the extracellular environment. Targeting this global event is important to gauge the pace of tumor growth and invasiveness, as well as to provide a basis for predicting disease response to pH-dependent chemotherapies. To realize this goal, a noninvasive method is necessary to measure tumor extracellular acidification to meet clinical needs. This study explores the utility of pH (low) insertion peptide, an acidosis-targeting peptide, as a PET-based imaging probe to provide a method for quantifying extracellular pH and its correlation to known acidity markers, such as hypoxia, carbonic anhydrase IX, and lactate dehydrogenase A, within the prostate tumor tissue.

Author contributions: N.T.V.-V., S.D.C., E.A., R.G.B., O.A.A., J.A.K., Y.K.R., and J.S.L. designed research; N.T.V.-V., S.D.C., E.A., K.K.S., V.D., I.S., N.K., and M.A. performed research; I.S. contributed new reagents/analytic tools; N.T.V.-V., S.D.C., E.A., I.S., J.A.K., and Y.K.R. analyzed data; and N.T.V.-V., S.D.C., E.A., I.S., R.G.B., D.M.E., J.A.K., Y.K.R., and J.S.L. wrote the paper.

The authors declare no conflict of interest.

[1] To whom correspondence may be addressed. E-mail: donald.engelman@yale.edu or lewisj2@mskcc.org.

This article contains supporting information online at www.pnas.org/lookup/suppl/doi:10.1073/pnas.1405240111/-/DCSupplemental.

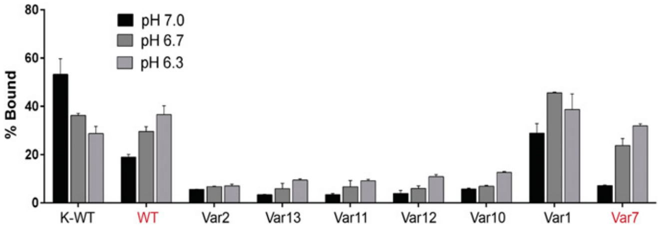

Fig. 1. ^{68}Ga-DOTA–labeled pHLIP variants. In vitro binding studies ($n = 3$) display higher binding of ^{68}Ga-DOTA-WT and ^{68}Ga-DOTA-Var7 variants as the pH of the incubation medium is decreased. Note that the opposite was observed with the control peptide, K-WT.

maintaining tumor specificity. Based on reports revealing that simple replacement of a radionuclide can significantly alter the PK characteristics of a PET probe (22, 23), we labeled WT and truncated versions of pHLIP from Scheme S1 with ^{68}Ga ($t_{1/2} \sim 68$ min) in lieu of ^{64}Cu ($t_{1/2} \sim 12.7$ h) with 1,4,7,10-tetraazacyclododecane-1,4,7,10-tetraacetic acid (DOTA) as chelate. Measurements of the octanol/water partition coefficient (Log P) showed that among the pHLIP variants tested, ^{68}Ga-DOTA-WT is the most hydrophilic (Log P ~ −2.26 ± 0.04), whereas ^{68}Ga-DOTA-Var7 is the most hydrophobic (Log P ~ −1.10 ± 0.05) (Table S1). The binding activity (expressed as "% Bound" normalized to the amount of probe added) of each radiolabeled variant (Fig. 1) in PC3-wt cells exposed in different pH environment showed that these peptides target cells at low pH. Variants WT and Var7 were selected as lead compounds for small animal PET imaging and biodistribution studies in vivo due to their differential but favorable binding at low pH and significantly lower uptake at neutral pH, resulting in an improved dynamic range/contrast in the pH range of interest (pH 6–7.4). The control peptide, K-WT, showed a reverse trend, with enhanced binding at high pH. The lysine residues in K-WT are in their charged form at low pH, inhibiting membrane insertion, although in a more alkaline environment, these lysine residues may be partially protonated, enhancing peptide–membrane interaction (24).

^{68}Ga-DOTA-WT vs. ^{68}Ga-DOTA-Var7. Encouraged by the results of our assays in vitro, we conducted in vivo experiments with s.c. PC3-wt prostate tumor xenografts using ^{68}Ga-DOTA-WT. Ex vivo tissue biodistribution analysis was conducted to measure the amount of probe bound to tumor and normal tissues to parallel the kinetics observed in the PET images. These data (Table S2) showed tumor uptake, expressed as the percentage of injected dose per gram of tissue (%ID/g) at 1 h (1.87 ± 0.45%ID/g), 2 h (2.36 ± 0.40%ID/g), and 4 h (2.86 ± 0.75%ID/g) postinjection (p.i.), in good agreement with previously reported data using ^{64}Cu, demonstrating probe affinity for the tumor (20). However, nonspecific binding of ^{68}Ga-DOTA-WT to normal tissues observed in the biodistribution results (Fig. 2*A* and Table S2) even at 4 h p.i. resulted in poor contrast. For example, tumor-to-healthy tissue ratios vs. muscle (2.02 ± 1.97), blood (0.43 ± 0.16), liver (0.40 ± 0.05), and kidneys (0.37 ± 0.16) at 4 h p.i. were poor, necessitating further improvement (Table 1).

The shorter ^{68}Ga-DOTA-Var7 variant was examined in the same PC3-wt tumor model using similar methods of preparation. Compared with the WT sequence, ^{68}Ga-DOTA-Var7 exhibited significantly improved properties. From the tissue distribution (Table S3), the probe accumulation within the tumor progressed from 2.47 ± 0.19%ID/g at 1 h p.i. to 5.60 ± 0.30%ID/g at 4 h p.i.

A direct comparative analysis between the two ^{68}Ga-labeled probes demonstrated a higher tumor uptake with the shorter sequence than with the parent WT. The blood residence at 4 h p.i. was similar; however, slightly increased nonspecific tissue binding was demonstrated by ^{68}Ga-DOTA-Var7 (Fig. 2*A*). Compared with the WT peptide, the kidney uptake for Var7 was elevated, which can be rationalized as resulting from faster probe clearance. Comparing tumor-to-background ratios of both radiotracers in Table 1, an overall increase in contrast with Var7 is seen. Based on these observations, Var7 was chosen as the lead pHLIP variant for further preclinical evaluation.

DOTA vs. 1,4,7-Triazacyclononane-1,4,7-Triacetic Acid. Even with shorter variants, the residence time of pHLIP appears longer than the physical $t_{1/2}$ of ^{68}Ga, so we reconsidered using ^{64}Cu to match the biological $t_{1/2}$ of pHLIP better. Ex vivo biodistribution results (Table S4) using PC3-wt tumor-bearing mice displayed tumor uptake at 1 h p.i. (1.19 ± 0.55%ID/g) and significant retention after 24 h (1.64 ± 0.38%ID/g; Fig. 2*B*). The blood residence activity improved with a final tumor-to-blood ratio of 2.63 ± 0.57 at 24 h p.i. (Table 1). Despite improvements made on the pHLIP backbone, concerns with radiotracer retention in key organs still remained. Hepatic uptake of the radiotracer displayed unremarkable retention over 24 h with 6.05 ± 1.36%ID/g (Fig. 2 *B* and *C*), similar to the values reported for the ^{64}Cu-DOTA-WT construct (4.88 ± 0.98%ID/g at 24 h) (20); this uptake is likely to be from random scavenging of radioactive metabolites, including demetallated ^{64}Cu in the liver (25). The tracer distribution in the kidney revealed only nominal reduction, even after 24 h (19.6 ± 4.0%ID/g), likely due to the renal acidic environment (pH ~5), which is expected to cause binding of these pHLIP variants for a period (26), but possibly including other effects, because it could be improved.

Our efforts to limit indiscriminate tissue accretion of pHLIP-PET probes led us to seek improvements of the radiometal/chelate stability and the resistance to proteolytic degradation. Var7 was modified with the 1,4,7-triazacyclononane-1,4,7-triacetic acid (NOTA) ligand because previous reports described superior chelate affinity for ^{64}Cu (27, 28). In addition, we used D-amino acids [henceforth called Var7(D)], which are known for their resistance to enzymatic proteolysis compared with L-peptidomimetics (29). In PC3-wt xenografts, no differences in tumor accretion were seen between ^{64}Cu-NOTA-Var7(D) (Fig. 2*B* and

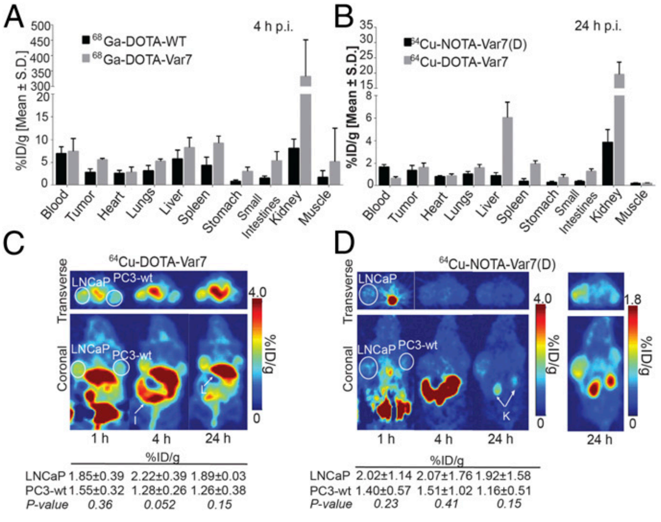

	%ID/g		
LNCaP	1.85±0.39	2.22±0.39	1.89±0.03
PC3-wt	1.55±0.32	1.28±0.26	1.26±0.38
P-value	*0.36*	*0.052*	*0.15*

	%ID/g		
LNCaP	2.02±1.14	2.07±1.76	1.92±1.58
PC3-wt	1.40±0.57	1.51±1.02	1.16±0.51
P-value	*0.23*	*0.41*	*0.15*

Fig. 2. In vivo pharmacokinetic optimization studies in prostate tumor xenografts. (*A*) Tissue distribution of ^{68}Ga-DOTA–labeled WT and Var7 demonstrates the superiority of Var7 in terms of tumor uptake at 4 h p.i. in PC3-wt tumor implants. (*B*) In the same tumor model, ^{64}Cu-NOTA-Var7(D) displays faster clearance and less nonspecific binding, particularly in hepatobiliary, intestinal, and renal tissues, in contrast to ^{64}Cu-DOTA-Var7. Tumor uptake of both probes was comparable at 24 h p.i. The PET images (*C* and *D*) of mice bearing dual LNCaP and PC3-wt tumors demonstrate the advantages of ^{64}Cu-NOTA-Var7(D) compared with ^{64}Cu-DOTA-Var7. The tumor uptake displayed in the tables is the mean ± SD of all acquired images ($n > 3$; i.e., with and without pHe measurements).

Table 1. Tumor-to-background tissue contrast ratios [mean ± SD (rel. u.)] obtained for the ^{68}Ga-labeled WT and Var7 variants at 4 h p.i. and for ^{64}Cu-Var7 with either DOTA or NOTA as a ligand at 24 h p.i

T/B	^{68}Ga-DOTA-WT	^{68}Ga-DOTA-Var7	^{64}Cu-DOTA-Var7	^{64}Cu-NOTA-Var7(D)
Tumor/blood	0.43 ± 0.16	0.69 ± 0.18	2.63 ± 0.57	0.81 ± 0.22
Tumor/liver	0.40 ± 0.05	0.61 ± 0.15	0.28 ± 0.08	1.56 ± 0.40
Tumor/kidney	0.37 ± 0.16	0.02 ± 0.01	0.08 ± 0.01	0.39 ± 0.17
Tumor/muscle	2.02 ± 1.97	3.17 ± 0.91	7.81 ± 1.78	7.81 ± 0.88
Tumor/bone	0.25 ± 0.13	0.57 ± 0.41	1.94 ± 0.41	6.04 ± 2.34

Absolute uptake values are listed in Table S2 for ^{68}Ga-DOTA-WT, Table S3 for ^{68}Ga-DOTA-Var7, Table S4 for ^{64}Cu-DOTA-Var7, and Table S5 for ^{64}Cu-NOTA-Var7(D). rel. u., relative units; T/B, tumor-to-background tissue.

Table S5) and the DOTA scaffold (Fig. 2*B* and Table S4). The design changes in ^{64}Cu-NOTA-Var7(D) resulted in significant improvements. First, renal accumulation showed greatly improved, exponential clearance from 13.27 ± 0.65%ID/g (1 h) to 5.84 ± 0.89%ID/g (4 h) and, finally, to 3.86 ± 1.14%ID/g (24 h). Second, a new route of clearance, via the intestinal organs, was found (Table S5). Third, negligible hepatic radiotracer retention was seen at 24 h (0.88 ± 0.26%ID/g; Fig. 2*B*). Finally, the significant clearance of ^{64}Cu-NOTA-Var7(D) from healthy tissues gave clear visualization of tumors as tumor-to-tissue contrasts (Table 1) progressed over 24 h, for example, against blood (0.81 ± 0.22), muscle (7.81 ± 0.88), liver (1.56 ± 0.40), small intestines (3.7 ± 1.0), and kidneys (0.39 ± 0.17). Compared with ^{64}Cu-DOTA-Var7 (Fig. 2*C*), PET images using ^{64}Cu-NOTA-Var7(D) acquired on mice implanted with bilateral s.c. PC3-wt (right shoulder) and LNCaP (left shoulder) xenografts exhibited promising PK properties (Fig. 2*D*) with progressive clearance of the tracer from the liver, muscle, gut, and kidneys over 24 h, which were key problem areas with previous pHLIP-PET probes.

Biophysical Characterization of ^{64}Cu-NOTA-Var7(D), Our Lead Compound. We tested the new compound, Cu-NOTA-Var7(D), for solubility and for pH-dependent insertion to form a transmembrane helix. Sedimentation velocity measurements show that Cu-NOTA-Var7(D) forms a dimer in aqueous solution at concentrations of 7–8 μM at high and neutral pH values. The pH-dependent changes in CD (Fig. 3*A*) and tryptophan fluorescence signals (Fig. 3*B*) are similar to those observed for the peptide with no chelate and metal (21), indicating pH-dependent interaction of the pHLIP portion with the membrane. The apparent pK_a of insertion was ~5.9 (Fig. 3*C*), which is slightly higher than for the peptide alone (pK_a = 5.5), probably due to the presence of the chelate. The Log P value of ^{64}Cu-NOTA-Var7(D) was measured as −2.45 ± 0.13, revealing a significant polar compound. The properties of increased solubility and elevation of the pK of insertion may contribute to its improved properties in vivo.

Probe Accumulation Correlates with Acidity. We wanted to explore disparities, if any, in the pHe of tumors with and without pHe regulators, particularly in tumors transduced to overexpress CAIX, a carbonic anhydrase elevated in tumor cells to cope with high CO_2 production. Thus, PC3-CAIX prostate cancer cells were established via the transduction of PC3-wt cells with a newly developed the retroviral vector SFG-CAIX-IRES2-GFP [retroviral vector derived from a murine leukemia virus (SFG)-CAIX-internal ribosomal entry site 2 (IRES2)-green fluorescent protein (GFP)] (30). Via cell sorting, populations of GFP-expressing cells were collected, (Fig. S1*A*) and Western blots confirmed higher CAIX expression in PC3-CAIX cells than in the WT cells under normal oxygenated conditions [20% (vol/vol) O_2] (Fig. S1*B*).

The intrinsic acidity of the three prostate xenografts (PC3-wt, PC3-CAIX, and LNCaP) was evaluated by measuring pHe and intracellular pH (pHi) via ^{1}H-decoupled ^{31}P magnetic resonance spectroscopy (MRS) using 3-aminopropylphosphonate (3-APP) (Fig. 4*A*). Each of the three tumor models exhibited a lower whole-tumor pHe (Fig. 4*B*) than its whole-tumor pHi (Fig. 4*C*), in concordance with previous studies (31–34). Of all of the tumor models, LNCaP tumors had the highest pHi (7.28 ± 0.07) and pHe (7.07 ± 0.04), whereas the PC3-wt xenografts exhibited the lowest pHi (6.94 ± 0.07) and pHe (6.93 ± 0.03). In contrast to the WT model, the CAIX-enhanced tumor implants displayed an alkaline-shifted pHi (7.26 ± 0.09, $P = 0.012$) and pHe (7.07 ± 0.06, $P = 0.035$). Analysis of the ΔpH (pHi − pHe) of these tumors revealed similar proton fluxes in LNCaP (0.27 ± 0.10, $P = 0.020$) and PC3-CAIX (0.33 ± 0.13, $P = 0.018$), establishing greater extracellular acidification gradients in these two xenografts than in PC3-wt (−0.010 ± 0.055) (Fig. 4*D*).

Uptake of ^{64}Cu-NOTA-Var7(D) correlates inversely with pHe when data from all three tumor models are taken into account. Each mouse used for pH MRS measurements was also used for PET and biodistribution experiments, giving greater confidence in the correlations (pairing details are provided in Table S6). In the plot of pHe vs. ^{64}Cu-NOTA-Var7(D) uptake (PET imaging at 1 h p.i. and 24-h ex vivo tissue sampling radioactivity assays) for PC3-wt tumors (Fig. 5*A*), incremental accumulation of the radiotracer is seen as the tumor acidity increases. By pooling all data points from all three prostate xenografts (Fig. 5*B*), threshold limits can be established, showing that a tumor pHe <6.9 provides high probe localization (>3.0%ID/g), whereas a pHe range of 6.9–7.4 results in lower probe uptake (<3.0%ID/g).

Ex Vivo Autoradiography Demonstrates pHLIP Accumulation in Tumor Regions Associated with Elevated Metabolism. Histological staining was used to examine viability and metabolic features of the tissues that stain or do not stain with the probe. Fig. 6 *A–C* shows the distribution of ^{64}Cu-NOTA-Var7(D) (autoradiography) and correlative histological markers pimonidazole (green, hypoxia), Hoechst 33342 (blue, vascular perfusion), and LDH-A (red) in representative PC3-CAIX (Fig. 6 *A–C*, *Top*), LNCaP (Fig. 6 *A–C*, *Middle*), and PC3-wt (Fig. 6 *A–C*, *Bottom*) tumors. Histological

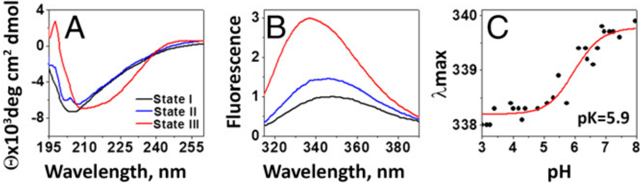

Fig. 3. pH-dependent interaction of Cu-NOTA-Var7(D) with the lipid membrane bilayer. Cold Cu-NOTA-Var7(D) was studied for the presence of the three basic states of pHLIP: State I is the peptide in solution at pH 8, state II is the peptide in the presence of 1-palmitoyl-2-oleoyl-sn-glycero-3-phosphocholine (POPC) liposomes at pH 8, and state III is the folding and insertion of the peptide with POPC liposomes from pH 8–3.6. The states were monitored by changes of the steady-state CD (*A*) and tryptophan fluorescence spectroscopy at λ_{ex} = 295 nm (*B*). (*C*) Changes in the intrinsic fluorescence were monitored as a function of pH wherein a pK_a of ~5.9 was obtained. λ_{max}, maximum wavelength.

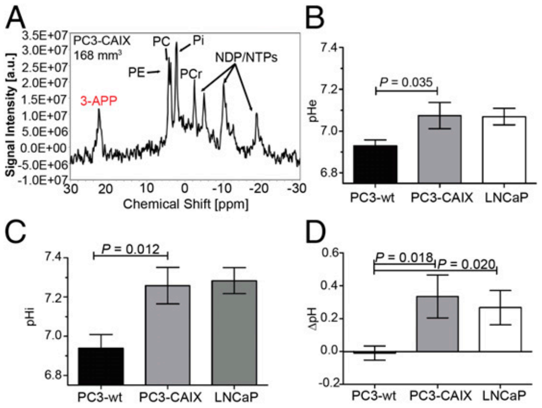

Fig. 4. In vivo pHe measurements. (*A*) Representative ^{1}H-decoupled ^{31}P MR spectrum of a PC3-CAIX tumor after 3-APP injection, where 3-APP, phosphoethanolamine (PE), phosphocholine (PC), P$_i$, phosphocreatine (PCr), NDP/NTPs. (*B*) pHe measurements show PC3-wt as the most acidic (6.93 ± 0.03; $P = 0.035$) compared with the PC3-CAIX (7.07 ± 0.06) and LNCaP (7.07 ± 0.04) xenografts. (*C*) Intracellular acidity of PC3-wt (6.94 ± 0.07; $P = 0.012$) is higher than that of the other prostate implants. (*D*) Positive proton fluxes are observed for PC3-CAIX (0.33 ± 0.13, $n = 5$; $P = 0.018$) and LNCaP (0.27 ± 0.10, $n = 5$; $P = 0.020$) tumors, but not for PC3-wt tumors (−0.010 ± 0.055, $n = 5$) (*D*). a.u., absorbance units.

stains (H&E) were also conducted to determine tumor tissue viability (Fig. S2). In all tumors, the ^{64}Cu-NOTA-Var7(D) distribution is heterogeneous, with increasing accumulation seen in perinecrotic, hypoxic tumor regions. Binding of ^{64}Cu-NOTA-Var7(D) is also observed in animal skin, an inherent acidic tissue, as indicated by the red arrows on the tumor sections in Fig. 6*B*. Fig. S3 *A–C* contains rebinned scatterplots of the relative pixel intensity values of the images shown in Fig. 6 *A–C*, respectively. In all cases, the regions of highest ^{64}Cu-NOTA-Var7(D) uptake corresponded with regions of highest pimonidazole and LDH-A staining, with the converse lowest ^{64}Cu-NOTA-Var7(D) uptake corresponding to the regions of lowest LDH-A expression and pimonidazole uptake. There appeared to be no relationship between Hoechst 33342 staining intensity and ^{64}Cu-NOTA-Var7(D) uptake. Thus, we find that probe uptake is correlated with hypoxia and LDH-A.

Discussion

By creating a useful probe for imaging tumor acidosis, we enable assessment of a universal trait associated with tumor invasiveness in most malignancies. We illustrate the improvements made toward better PK and dosimetric properties of pHLIP as a noninvasive PET radiotracer. More importantly, this probe was able to distinguish highly acidic tumors, with a direct association to tumor pHe. Furthermore, we extended our efforts at understanding the mechanism of uptake of this probe through autoradiographic and histological studies of all three tumor models to provide insights on its target.

Based on a set of observations with earlier pHLIP-based probes, we were able to design a new version that should prove useful in clinical applications. The Var7 variant sequence of pHLIP proved to offer faster clearance and tumor delivery than the parent pHLIP; however, its prolonged residence in healthy tissue, paired with the short physical $t_{1/2}$ of ^{68}Ga, was mismatched, and degradation of the peptide was suspected. To cope with these issues, we synthesized the peptide from D-amino acids and revisited the use of ^{64}Cu, which has a longer $t_{1/2}$, to allow clearance of the probe from healthy tissue. The relatively poor chelating properties of DOTA for ^{64}Cu had resulted in accumulation of unbound Cu in tissues (i.e., liver) (25), so we searched for a better chelation group, deciding on NOTA. This set of design choices gave us ^{64}Cu-NOTA-Var7(D). The superiority of NOTA to DOTA is clear in the comparisons of biodistribution, tumor-to-tissue contrast ratios, and PET imaging (Fig. 2 *C* and *D* and Tables S4 and S5). A much lower uptake is seen in the liver, intestines, spleen, and kidneys, resulting in improved contrast ratios between these tissues and the tumor. We now have a workable probe to develop for clinical use.

Our results differ in some respects from those reported earlier. In our hands, in a comparison of two of the tumor models (LNCaP and PC3-wt) in the right shoulder of athymic nude mice, the pHe showed a trend opposite to that observed by Vāvere et al. (20). Those investigators also used LNCaP and PC3, but for tumors implanted in the flanks of athymic nu/nu mice and for tumor volumes >500 mm^3, so the observed differences may potentially be due to the smaller tumor size (<400 mm^3) used in our study and the differences in tumor location (shoulder vs. flank). Our goal was to use tumors with only moderate necrosis for the best comparison with tumors seen in the clinic; hence, our choice of small- to medium-sized tumors. Further, we used ^{1}H-decoupled ^{31}P MRS, which may influence the average chemical shift of 3-APP, because without ^{1}H decoupling, the signal shape and width are not only determined by T2 relaxation and the pHe tissue distribution but also by the multiplet structure of 3-APP (35). We did not find a significant relationship between tumor size and pHe for tumors <400 mm^3 (Table S6), which is consistent with the data by Raghunand et al. (34), in which tumoral pH was observed to decrease over a tumor size range of ∼200—1,500 mm^3, although not significantly decreasing in smaller tumors (<400 mm^3). Although decreases of mean tumor pHe and pHi with increasing tumor size have been observed in rodent tumors when measured over a large tumor size range (32, 34), both decreasing pH with increasing tumor size and a lack of such a relationship have been reported in human tumors (36).

In retrospect, we find that the outcomes of measuring pH as an average do not give a true representation of tumor acidity, as evidenced by the broad pH distributions observed from ^{31}P MRS. Instead, details of pH variation within a tumor may be key, even at the cellular level. Variations in the spatial distribution of pHe have been reported such that gradients exist at the interface of the cellular membrane and cytosol (37, 38), prompting us to examine the differences between cytosolic and extracellular pH and to derive the net proton flux (although we still needed to use average values). We observed that the transduced PC3-CAIX and LNCaP implants had greater pHe gradients (ΔpH) than the WT (PC3-wt) model; however, the measured pHe values of the two models followed an opposite trend from the ΔpH values. We rationalize that these contrasting measurements may be due to the vast heterogeneity in tumor homeostasis and development, which is governed by an intricate mesh of metabolic pathways, including rate of glycolytic metabolism, expression of acid-extruding protein, and diverse buffering capacities and O$_2$

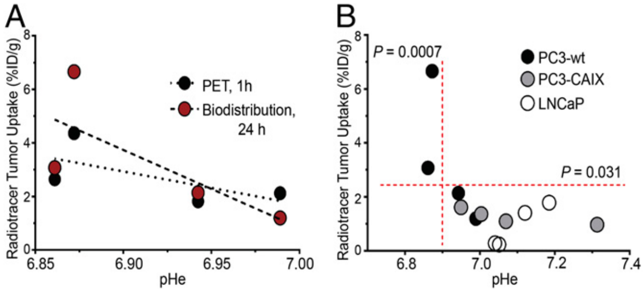

Fig. 5. pHLIP-PET shows a direct association with extracellular acidity. (*A*) ^{64}Cu-NOTA-Var7(D) tumor uptake is shown to increase as the pHe of the PC3-wt tumor model decreases. (*B*) Plot of the pHe against radiotracer tumor uptake (24 h p.i.) from all three tumor models demonstrates a notable threshold where higher probe accretion (>3%ID/g) correlates to an acidic extracellular space with pHe <6.9. Because of tumor heterogeneity even within the same xenograft model, each measured tumor is treated as a separate data point.

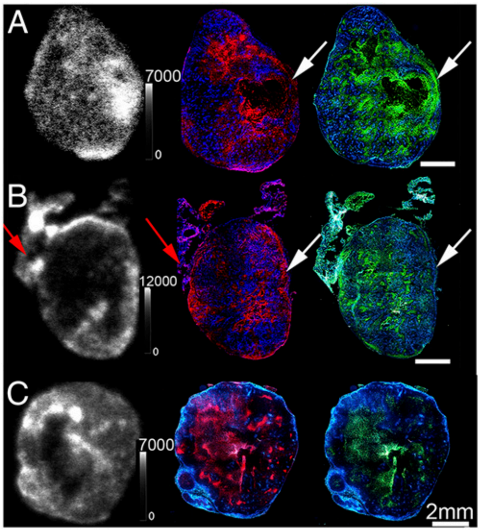

Fig. 6. Histology and autoradiography. ^{64}Cu-NOTA-Var7(D) autoradiography (24 h p.i.) and correlative histology from 10-μm adjacent sections obtained from PC3-CAIX (*A*), LNCaP (*B*), and PC3-wt (*C*) tumors. The distributions of ^{64}Cu-NOTA-Var7(D) (white), pimonidazole (hypoxia, green), and Hoechst 33342 (perfusion, blue), as well as the expression of LDH-A (red), are shown. White arrows indicate discordance between pimonidazole uptake and LDH-A expression, whereas red arrows mark skin accumulation of the imaging probe.

concentrations in the blood vessel network, just to name a few factors (36, 39). Despite these uncertainties, we observed a correlation of targeting with absolute pHe, where, at a pHe <6.9, higher tumor accumulation of the radiotracer was observed, with >3%ID/g. However, at a pHe >6.9, measuring and imaging tumor acidity using this probe is poorly resolved. We postulate that this incident may be an effect of the insertion pK_a of the full construct ($pK_a \sim 5.9$).

The development and use of pHLIP variants with higher and lower pK_as of insertion across cellular membranes, combined with favorable thermodynamics and kinetics properties, would allow measurement of a wider dynamic range of potential pHe probed by pHLIP technology. Also, pHLIP variants tuned over a pK_a range could expand the applicability of minimally invasive pH measurements to applications beyond cancer. Thus, pHLIP-based acidosis imaging probes may offer a relative read-out of distributions of pHe, which may, in turn, allow clinical analysis of tumor invasiveness and regionalization. As we move forward, associating pHLIP tumor uptake with tumor acidosis using a regional pHe map is deemed more appropriate; these studies are currently underway.

Autoradiography and histology performed on excised tumor sections revealed a heterogeneous distribution of ^{64}Cu-NOTA-Var7(D) within the tumors, again emphasizing the need to avoid gross averaging of pH measurements solely to correlate the target(s) of our probe with markers related to acidity. We used pimonidazole (a hypoxia tracer) and LDH-A (involved in the interconversion of pyruvate and lactate) (40) as markers for comparison with the pHLIP distribution, in the absence of a direct histological marker of low pHe. ^{64}Cu-NOTA-Var7(D) localization appears preferentially in perinecrotic regions (Fig. S2) that display high uptake of the hypoxia marker pimonidazole but shows no clear relationship with the vascular perfusion marker Hoechst 33342 (Fig. S3). Elevated LDH-A would be expected to result in concomitant elevated pHLIP binding, which we have observed in all three tumor models (Fig. S3).

Our data demonstrate that in the tumor models used in this study, LDH-A expression and pimonidazole binding (primarily dependent on low pO_2) (41) have similar but discordant spatial distributions, in good agreement with previous reports that lactic acidosis and hypoxia are not always interdependent (9, 38, 39). It is likely that tumor regions of poor vascularity and low pO_2 will also possess excess extracellular H^+ ions due to anaerobic glucose metabolism and local lactic acidosis. Although we observed a trend toward increasing ^{64}Cu-NOTA-Var7(D) uptake with increasing pimonidazole uptake, the relationship appears to be nonlinear (Fig. S3 *A*–*C*). This observation may be due, in part, to the effect of pHe on absolute pimonidazole uptake, although this observation is likely to be a minor effect over the pHe ranges measured in this study (42).

CAIX expression, which can be taken to indicate regions of lowered pHe, is similarly regulated by HIF-1 transcription factor and has a cellular $t_{1/2}$ in the order of days (43). Although arguably inversely related to lowered pHe, CAIX expression cannot be assumed to relate to absolute pHe linearly. Taken together with the induced, constitutive expression in the PC3-CAIX model and the very low observed CAIX expression in the LNCaP model, these facts render CAIX an unsuitable marker for low pHe or pO_2 in our study.

By finding a probe that marks the acidosis inherent in tumor metabolism, we have defined a clinical potential for marking tumors and measuring their aggressive characteristics. Defining a probe with usable imaging properties could allow it to be used to follow the progression of a tumor and to monitor the effects of therapy.

Methods

Additional details of materials, methods, and equipment can be found in *SI Methods*.

Radiochemistry. Variants of pHLIP were purchased from C. S. Bio Co., Inc. and derivatized with either maleimido-monoamide-DOTA (Macrocyclics, Inc.) or *p*-SCN-Bn-NOTA (Macrocyclics, Inc.). Radiolabeling of pHLIP-DOTA or pHLIP-NOTA with ^{68}Ga or ^{64}Cu was conducted via a microwave-assisted reaction at 90 °C for 1 min in 0.5 M ammonium acetate (pH ~5.5). Unbound radiometal was removed via a C18 solid-phase extraction cartridge (Grace). The pure labeled peptide was eluted with 0.5% 2 M HCl in ethanol. Radiochemical purities of >95% were ensured before administration to animals.

In Vitro Cell Binding. PC3-wt cells were incubated with different ^{68}Ga-labeled pHLIP-DOTA variants for 1 h at 37 °C at different pH values ranging from ~6.3 to 7.0. The cells were then washed twice with the same media used for incubation to remove unbound activity, and the retained activity was counted using a Wizard^2 2480 gamma counter (PerkinElmer).

pH Dependence. The pH-dependent partitioning of the peptides into lipid bilayers using 1-palmitoyl-2-oleoyl-sn-glycero-3-phosphocholine liposomes was investigated by measuring the shift of the intrinsic fluorescence spectral maximum of the peptide as the pH is lowered from pH 8 to pH 2, as previously described (21).

Steady-State Fluorescence and CD Measurements. Tryptophan fluorescence and CD measurements were carried out on a PC1 ISS spectrofluorometer (ISS, Inc.) and a MOS-450 spectrometer (Biologic, Inc.), respectively, at 25 °C, as previously reported (21).

Partition Coefficient. The Log P values (n = 3) were determined for each labeled peptide by measuring the amount of activity from an equal volume of samples obtained from the octanol and 1× PBS (pH ~7) layers.

Cell Transduction. Stable clones of PC3-CAIX were developed by transducing PC3-wt cells with SFG-CAIX-IRES2-GFP. PC3-wt cells at ~50% confluence were incubated with virus-containing medium for 12 h in the presence of Polybrene (8 mg/mL; Sigma) as previously described (44). Cells were sorted several times using a FACS (BD Bioscience) (Fig. S1*A*), with Western blot experiments confirming CAIX expression (Fig. S1*B*).

Animal Models. All animals were treated according to the guidelines set and approved by the Research Animal Resource Center and Institutional Animal Care and Use Committee at Memorial Sloan–Kettering Cancer Center. Tumors were induced in male, athymic nu/nu mice (Taconic Farms, Inc. or Harlan Laboratories) on the shoulder by s.c. injection of 3 × 10^6 million cells of PC3-wt, PC3-CAIX, or LNCaP cells in a 200-μL suspension of 1:1 media/Matrigel Basement Membrane Matrix (BD Sciences). Mice were used once tumor volumes reached 150–300 mm^3.

In Vivo Animal PET Imaging and Biodistribution. Mice (n = 3–5) were injected i.v. with ^{68}Ga/^{64}Cu-pHLIP variants (200–300 μCi, 15–25 μg for imaging and 20–50 μCi, 1–2 μg for biodistribution) in 100–200 μL of 0.9% saline formulations. Imaging experiments were recorded with a microPET Focus 120 or R4 scanner (Concorde Microsystems) at 1–24 h p.i., while the mice were anesthetized with 1.5–2.0% isoflurane (Baxter Healthcare) in air. The images were analyzed for regions of interest (ASIPro VM; Concorde Microsystems). Biodistribution studies were conducted after the mice were killed via CO_2 asphyxiation 1–24 h p.i. The %ID/g was calculated as the activity bound to the tissue per organ weight per actual injected dose and was decay-corrected to the time of counting. For studies demonstrating correlation of extracellular acidification and pHLIP-PET, pH, PET imaging, and biodistribution measurements were conducted on the same tumors. Using the same mice, ^{64}Cu-NOTA-Var7(D) was administered i.v. post-MRS. PET images were acquired at 1–24 h p.i., with the mice subsequently euthanized after the last scan for ex vivo tissue analysis. Pairing of tumors is detailed in Table S6.

In Vivo pH Measurements by ^{1}H-Decoupled ^{31}P MRS. The MRS experiments were performed on a horizontal-bore 7-T MR spectrometer (Bruker) using a home-built ^{1}H/^{31}P magnetic resonance (MR) coil assembly, using previous methods (35, 45) (*SI Methods*). The MR spectra were fitted in the time domain, using the software XsOsNMR (kindly provided by Dr. Dikoma Shungu and Xiaoling Mao, Cornell University, New York). The intracellular and extracellular pH (pHi, pHe) were calculated from the chemical shifts (δ) of inorganic phosphate (Pi) and 3-aminopropylphosphonate (3-APP) relative to α-NTP at −10.05 ppm, respectively, using their respective Henderson-Hasselbalch equations (*SI Methods*) as described previously (35). As Pi is predominantly intracellular (45), the resulting calculated pH represents the pHi (35). The pH values were reported as the mean ± SEM.

Statistical Analysis. Data values were expressed as the mean ± SD unless otherwise stated. Statistical analysis was performed with GraphPad Prism version 5.03 software using the Student t test. A P value of <0.05 is considered statistically significant.

ACKNOWLEDGMENTS. We thank Dr. Pat Zanzonico, Dr. Alexander Karabadzhak, Valerie Longo, Blesida Punzalan, Nicholas Ramos, Charles Davis, and the Radiochemistry and Molecular Imaging Core for technical assistance. This work was funded by National Institutes of Health (NIH) Grant R01 CA138468 (to J.S.L.). Funding support was also provided by NIH Small Animal Imaging Research Program Grant R24-CA83084 and Memorial Sloan–Kettering Cancer Center Grant P30-CA08748.

1. Gottfried E, Kreutz M, Mackensen A (2012) Tumor metabolism as modulator of immune response and tumor progression. *Semin Cancer Biol* 22(4):335–341.
2. Vander Heiden MG, Cantley LC, Thompson CB (2009) Understanding the Warburg effect: The metabolic requirements of cell proliferation. *Science* 324(5930):1029–1033.
3. Chiche J, Brahimi-Horn MC, Pouysségur J (2010) Tumour hypoxia induces a metabolic shift causing acidosis: A common feature in cancer. *J Cell Mol Med* 14(4):771–794.
4. Guillaumond F, et al. (2013) Strengthened glycolysis under hypoxia supports tumor symbiosis and hexosamine biosynthesis in pancreatic adenocarcinoma. *Proc Natl Acad Sci USA* 110(10):3919–3924.
5. Park HJ, Lyons JC, Ohtsubo T, Song CW (1999) Acidic environment causes apoptosis by increasing caspase activity. *Br J Cancer* 80(12):1892–1897.
6. Williams AC, Collard TJ, Paraskeva C (1999) An acidic environment leads to p53 dependent induction of apoptosis in human adenoma and carcinoma cell lines: Implications for clonal selection during colorectal carcinogenesis. *Oncogene* 18(21):3199–3204.
7. Neri D, Supuran CT (2011) Interfering with pH regulation in tumours as a therapeutic strategy. *Nat Rev Drug Discov* 10(10):767–777.
8. Zhang X, Lin Y, Gillies RJ (2010) Tumor pH and its measurement. *J Nucl Med* 51(8):1167–1170.
9. Mazzio EA, Boukli N, Rivera N, Soliman KF (2012) Pericellular pH homeostasis is a primary function of the Warburg effect: Inversion of metabolic systems to control lactate steady state in tumor cells. *Cancer Sci* 103(3):422–432.
10. de Groof AJ, et al. (2009) Increased OXPHOS activity precedes rise in glycolytic rate in H-RasV12/E1A transformed fibroblasts that develop a Warburg phenotype. *Mol Cancer* 8:54.
11. Wu M, et al. (2007) Multiparameter metabolic analysis reveals a close link between attenuated mitochondrial bioenergetic function and enhanced glycolysis dependency in human tumor cells. *Am J Physiol Cell Physiol* 292(1):C125–C136.
12. Gatenby RA, Gillies RJ (2004) Why do cancers have high aerobic glycolysis? *Nat Rev Cancer* 4(11):891–899.
13. Carmeliet P, et al. (1998) Role of HIF-1alpha in hypoxia-mediated apoptosis, cell proliferation and tumour angiogenesis. *Nature* 394(6692):485–490.
14. Jang A, Hill RP (1997) An examination of the effects of hypoxia, acidosis, and glucose starvation on the expression of metastasis-associated genes in murine tumor cells. *Clin Exp Metastasis* 15(5):469–483.
15. Estrella V, et al. (2013) Acidity generated by the tumor microenvironment drives local invasion. *Cancer Res* 73(5):1524–1535.
16. An M, Wijesinghe D, Andreev OA, Reshetnyak YK, Engelman DM (2010) pH-(low)-insertion-peptide (pHLIP) translocation of membrane impermeable phalloidin toxin inhibits cancer cell proliferation. *Proc Natl Acad Sci USA* 107(47):20246–20250.
17. Moshnikova A, Moshnikova V, Andreev OA, Reshetnyak YK (2013) Antiproliferative effect of pHLIP-amanitin. *Biochemistry* 52(7):1171–1178.
18. Daumar P, et al. (2012) Efficient (18)F-labeling of large 37-amino-acid pHLIP peptide analogues and their biological evaluation. *Bioconjug Chem* 23(8):1557–1566.
19. Andreev OA, et al. (2010) pH (low) insertion peptide (pHLIP) inserts across a lipid bilayer as a helix and exits by a different path. *Proc Natl Acad Sci USA* 107(9):4081–4086.
20. Vāvere AL, et al. (2009) A novel technology for the imaging of acidic prostate tumors by positron emission tomography. *Cancer Res* 69(10):4510–4516.
21. Weerakkody D, et al. (2013) Family of pH (low) insertion peptides for tumor targeting. *Proc Natl Acad Sci USA* 110(15):5834–5839.
22. Antunes P, et al. (2007) Are radiogallium-labelled DOTA-conjugated somatostatin analogues superior to those labelled with other radiometals? *Eur J Nucl Med Mol Imaging* 34(7):982–993.
23. Wadas TJ, Wong EH, Weisman GR, Anderson CJ (2010) Coordinating radiometals of copper, gallium, indium, yttrium, and zirconium for PET and SPECT imaging of disease. *Chem Rev* 110(5):2858–2902.
24. Andreev OA, et al. (2007) Mechanism and uses of a membrane peptide that targets tumors and other acidic tissues in vivo. *Proc Natl Acad Sci USA* 104(19):7893–7898.
25. Bass LA, Wang M, Welch MJ, Anderson CJ (2000) In vivo transchelation of copper-64 from TETA-octreotide to superoxide dismutase in rat liver. *Bioconjug Chem* 11(4):527–532.
26. Feng B, LaPerle JL, Chang G, Varma MV (2010) Renal clearance in drug discovery and development: Molecular descriptors, drug transporters and disease state. *Expert Opin Drug Metab Toxicol* 6(8):939–952.
27. Ait-Mohand S, et al. (2011) Evaluation of 64Cu-labeled bifunctional chelate-bombesin conjugates. *Bioconjug Chem* 22(8):1729–1735.
28. De Silva RA, et al. (2012) Copper-64 radiolabeling and biological evaluation of bifunctional chelators for radiopharmaceutical development. *Nucl Med Biol* 39(8):1099–1104.
29. Fischer PM (2003) The design, synthesis and application of stereochemical and directional peptide isomers: A critical review. *Curr Protein Pept Sci* 4(5):339–356.
30. Riviere I, Brose K, Mulligan RC (1995) Effects of retroviral vector design on expression of human adenosine deaminase in murine bone marrow transplant recipients engrafted with genetically modified cells. *Proc Natl Acad Sci USA* 92(15):6733–6737.
31. Gillies RJ, Raghunand N, Garcia-Martin ML, Gatenby RA (2004) pH imaging. A review of pH measurement methods and applications in cancers. *IEEE Eng Med Biol Mag* 23(5):57–64.
32. Gillies RJ, Raghunand N, Karczmar GS, Bhujwalla ZM (2002) MRI of the tumor microenvironment. *J Magn Reson Imaging* 16(4):430–450.
33. Vaupel P, Kallinowski F, Okunieff P (1989) Blood flow, oxygen and nutrient supply, and metabolic microenvironment of human tumors: A review. *Cancer Res* 49(23):6449–6465.
34. Raghunand N, et al. (1999) Plasmalemmal pH-gradients in drug-sensitive and drug-resistant MCF-7 human breast carcinoma xenografts measured by 31P magnetic resonance spectroscopy. *Biochem Pharmacol* 57(3):309–312.
35. Raghunand N (2006) Tissue pH measurement by magnetic resonance spectroscopy and imaging. *Methods Mol Med* 124:347–364.
36. Tannock IF, Rotin D (1989) Acid pH in tumors and its potential for therapeutic exploitation. *Cancer Res* 49(16):4373–4384.
37. Paradise RK, Whitfield MJ, Lauffenburger DA, Van Vliet KJ (2013) Directional cell migration in an extracellular pH gradient: A model study with an engineered cell line and primary microvascular endothelial cells. *Exp Cell Res* 319(4):487–497.
38. Helmlinger G, Yuan F, Dellian M, Jain RK (1997) Interstitial pH and pO2 gradients in solid tumors in vivo: High-resolution measurements reveal a lack of correlation. *Nat Med* 3(2):177–182.
39. Molavian HR, Kohandel M, Milosevic M, Sivaloganathan S (2011) Deriving mechanisms responsible for the lack of correlation between hypoxia and acidity in solid tumors. *PLoS ONE* 6(12):e28101.
40. Chen JL, et al. (2008) The genomic analysis of lactic acidosis and acidosis response in human cancers. *PLoS Genet* 4(12):e1000293.
41. Arteel GE, Thurman RG, Yates JM, Raleigh JA (1995) Evidence that hypoxia markers detect oxygen gradients in liver: Pimonidazole and retrograde perfusion of rat liver. *Br J Cancer* 72(4):889–895.
42. Kleiter MM, et al. (2006) A comparison of oral and intravenous pimonidazole in canine tumors using intravenous CCI-103F as a control hypoxia marker. *Int J Radiat Oncol Biol Phys* 64(2):592–602.
43. Russell J, et al. (2009) Immunohistochemical detection of changes in tumor hypoxia. *Int J Radiat Oncol Biol Phys* 73(4):1177–1186.
44. Serganova I, et al. (2004) Molecular imaging of temporal dynamics and spatial heterogeneity of hypoxia-inducible factor-1 signal transduction activity in tumors in living mice. *Cancer Res* 64(17):6101–6108.
45. Soto GE, Zhu Z, Evelhoch JL, Ackerman JJ (1996) Tumor 31P NMR pH measurements in vivo: A comparison of inorganic phosphate and intracellular 2-deoxyglucose-6-phosphate as pHnmr indicators in murine radiation-induced fibrosarcoma-1. *Magn Reson Med* 36(5):698–704.